DOI: https://doi.org/10.2138/am-2022-8800. http://www.minsocam.org/

Revision 1

Yakubovichite, $CaNi_2Fe^{3+}(PO_4)_3$, a new nickel phosphate mineral of non-meteoritic origin

Sergey N. Britvin[1,2]*, Mikhail N. Murashko[1], Maria G. Krzhizhanovskaya[1], Yevgeny Vapnik[3], Natalia S. Vlasenko[4], Oleg S. Vereshchagin[1], Dmitrii V. Pankin[5], Anatoly N. Zaitsev[1], and Anatoly A. Zolotarev[1]

[1]Institute of Earth Sciences, Saint-Petersburg State University, Universitetskaya Nab. 7/9, St. Petersburg, 199034, Russia.

[2]Nanomaterials Research Center, Kola Science Center, Russian Academy of Sciences, Fersman Str. 14, Apatity, 184200, Russia.

[3]Department of Geological and Environmental Sciences, Ben-Gurion University of the Negev, POB 653, Beer-Sheva, 84105, Israel.

[4]Geomodel Resource Center, Saint-Petersburg State University, Ulyanovskaya Str. 1, St. Petersburg, 198504, Russia.

[5]Center for Optical and Laser Materials Research, St. Petersburg State University, Ulyanovskaya Str. 5, St. Petersburg, 199034, Russia

* Corresponding author. E-mail: sergei.britvin@spbu.ru

Abstract

Yakubovichite, $CaNi_2Fe^{3+}(PO_4)_3$, a new mineral containing up to 20 wt.% NiO, represents a novel type of terrestrial phosphate mineralisation featuring an extreme enrichment in Ni. The mineral was discovered in the Hatrurim Formation (Mottled Zone) – pyrometamorphic complex whose outcrops are exposed in Israel and Jordan in the area coincident with the Dead Sea Transform fault system. Nickel-rich minerals in these assemblages also include Ni phosphides: halamishite Ni_5P_4, negevite NiP_2, transjordanite and orishchinite – two polymorphs of Ni_2P, nazarovite $Ni_{12}P_5$, polekovskyite $MoNiP_2$; Ni-spinel trevorite $NiFe_2O_4$, bunsenite NiO, and nickeliferous members of the hematite-eskolaite series, Fe_2O_3-Cr_2O_3 containing up to 2 wt.% NiO. Yakubovichite forms polycrystalline segregations up to 0.2 mm in size composed of equant crystal grains, in association with crocobelonite, hematite, other phosphates and phosphides. It has a deep yellow to lemon-yellow colour; transparent to translucent with vitreous luster, with no cleavage. Mohs hardness = 4. Yakubovichite is orthorhombic, *Imma*, unit cell parameters of the holotype material: *a* 10.3878(10), *b* 13.0884(10), *c* 6.4794(6) Å, *V* 880.94(2) $Å^3$, $Z = 4$. Chemical composition of holotype material (electron microprobe, wt.%): Na_2O 1.82, K_2O 1.76, CaO 6.37, SrO 0.49, BaO 1.37, MgO 2.13, NiO 21.39, CuO 0.16, Fe_2O_3 18.80, Al_2O_3 1.06, V_2O_3 0.44, Cr_2O_3 0.15, P_2O_5 44.15, total 100.09. The empirical formula calculated on the basis of 12 oxygen atoms per formula unit is: $(Ca_{0.55}Na_{0.29}K_{0.18}Ba_{0.04}Sr_{0.02})_{1.08}(Ni_{1.39}Mg_{0.26}Fe^{3+}_{0.24}V^{3+}_{0.03}Cu_{0.01}Cr_{0.01})_{\Sigma 1.94}(Fe^{3+}_{0.90}Al_{0.10})_{\Sigma 1}P_{3.02}O_{12}$. $D_{calc.} = 3.657$ g cm^{-3}. The strongest lines of powder XRD pattern [*d*(Å)(*I*)(*hkl*)]: 5.82(44)(011), 5.51(73)(101), 5.21(32)(200), 4.214(34)(121), 2.772(97)(240), 2.748(100)(202), 2.599(38)(400). Yakubovichite is the first mineral that crystallizes in the α-$CrPO_4$ structure type. It has a direct synthetic analogue, $CaNi_2Fe^{3+}(PO_4)_3$. Since yakubovichite is the first natural Ni-phosphate of non-meteoritic origin, the possible sources of Ni in the reported mineral assemblages are discussed. Pyrometamorphic rocks of the Hatrurim Formation were formed at the expense of the sediments

DOI: https://doi.org/10.2138/am-2022-8800. http://www.minsocam.org/

belonging to a Cretaceous-Paleogene (Cretaceous-Tertiary) boundary (~66 Ma age). This geological frame marks the event of mass extinction of biological species on Earth that was likely caused by the Chicxulub impact event. The anomalous enrichment of pyrometamorphic assemblages in Ni may be related to metamorphic assimilation of Ni-rich minerals accumulated in the Cretaceous-Paleogene layer, which was formed due to a Chicxulub collision.

Keywords: nickel, phosphate, phosphide, trevorite, bunsenite, escolaite, crystal structure, pyrometamorphism, Dead Sea Transform Fault, Hatrurim Formation, Cretaceous-Paleogene boundary

Introduction

Nickel in metallogenic provinces on Earth behaves as a typical chalcophile element, with a strong affinity to sulfide and arsenide ores (Meyer 1968). The world largest Cu-Ni-PGE sulfide deposits that are confined to ultrabasic complexes, such as Norilsk-Talnakh in Russia (Barnes et al. 2020), Sudbury in Canada (Hawley 1962), Cu-Ni ore fields in Australia (Hoatson et al. 2006), as well as Ni-laterites formed by the weathering of sulfide-bearing ultramafites (Thorne et al. 2012) provide ~90% of Ni world production (Meyer 1968). In XIX-XX centuries, Ni deposits belonging to a so-called five-element, or Ag–Bi–Co–Ni–U formation, with predominance of Ni-Co arsenide ores, were very important. The ore fields of this type are widespread in Canada (Petruk 1971). However, the most famous and best studied five-element mining district is an Erzgebirge area, which encompasses numerous, now abandoned shafts in Saxony (Germany) and Jáchymov (St. Joachimsthal) in Czech Republic (Ondruš et al. 2003; Guilcher et al. 2021).

The speciation of secondary minerals in the oxidation zones of ore deposits is largely determined by the composition of primary ores. Therefore, it is not surprising that the most diverse group among secondary Ni minerals is arsenates, counting 17 valid species (www.mindat.org, accessed August 2022). One could expect that phosphorus, as a nearest chemical analogue of arsenic, could also couple with Ni in the oxidation zone to form corresponding phosphates. However, there were only two Ni phosphate minerals reported until last decade – cassidyite, $Ca_2Ni(PO_4)_2{\cdot}2H_2O$, and arupite $Ni_3(PO_4)_2{\cdot}8H_2O$. Both minerals have rather exotic origin – they are the products of terrestrial weathering of iron meteorites. Cassidyite was discovered among secondary mineral assemblages of the Wolf Creek meteorite crater in Victoria, Western Australia (White et al. 1967), whereas arupite originates from the oxidation crust of the world biggest Ni-rich ataxite – the Santa Catharina meteorite, Brazil (Buchwald 1975; 1990). Recently, we briefly introduced the readers with a novel type of terrestrial phosphate mineralization – the assemblages formed by pyrolytic oxidation of natural phosphides in the Hatrurim Formation, the area confined to the Dead Sea Transform fault system (Britvin et al. 2021a). The specific feature of reported associations is an anomalous enrichment in Ni. In the present paper, we provide the first mineralogical description of a new Ni phosphate from these localities. The mineral is named yakubovichite (cyrillic spelling - якубовичит), in honor of Prof. Olga Vsevolodovna Yakubovich (born 1950), a prominent Russian crystal chemist, for her contributions to the studies of inorganic phosphates. Olga Yakubovich is an author of more than 100 articles devoted to the crystal chemistry of phosphates (e.g., Yakubovich et al. 2021 and other articles). The mineral and its name have been approved by the Commission on New Minerals, Nomenclature and Classification (CNMNC) of the International Mineralogical Association (IMA 2020-094). The holotype specimen of yakubovichite is deposited in the collections of the Fersman Mineralogical Museum of the Russian Academy of Sciences, Moscow, Russia, with the registration number 5626/1.

Analytical methods

Electron microprobe analysis

Chemical composition of yakubovichite and associated minerals was determined on polished and carbon-coated thin sections using an INCA WAVE 500 WDX spectrometer (20 kV, 10 nA) attached to a Hitachi S-3400N SEM. The following standards were used ($K\alpha$ lines): chkalovite (Na), diopside (Ca, Si), microcline (K), celestine (Sr), cuprite (Cu), chromite (Cr), V_2O_3 (V), hematite (Fe), trevorite (Ni), gehlenite (Al), rutile (Ti), Co metal (Co), and chlorapatite (P). Ba$L\alpha$ was measured with barite.

Single-crystal X-ray diffraction (SCXRD) and powder diffraction (PXRD)

SCXRD data collection was performed with a Bruker Kappa APEX DUO CCD diffractometer (microfocus tube, Mo$K\alpha$ radiation). Subsequent data processing and integration procedures were carried out using Rigaku Oxford Diffraction CrysAlisPro software (Rigaku Oxford Diffraction). The crystal structure was solved and refined to R_1 = 0.029 using *SHELX*-2018 program package (Sheldrick 2015) incorporated into Olex2 graphic user shell (Dolomanov et al. 2009). The complete set of data collection and structure refinement details can be retrieved from crystallographic information file (CIF) in Supplementary Data. PXRD patterns of yakubovichite and bunsenite were acquired using a Rigaku RAXIS Rapid II diffractometer. The instrument uses rotating anode (Co*K*α, 40 kV, 15 mA), microfocus mirror monochromator and semi-cylindrical imaging plate detector (*r* = 127.4 mm), and is set up in the Debye-Scherrer geometry. A plate-to-profile data conversion was carried out with osc2xrd program (Britvin et al. 2017). The unit-cell parameters refinement and theoretical pattern calculation was performed with Stoe WinXPOW software (Stoe and Cie GmbH).

Raman spectroscopy

The Raman spectrum of yakubovichite was obtained by means of a LabRam HR 800 (Horiba Jobin–Yvon) Raman spectrometer with He-Ne laser excitation (632.8 nm). The ~1mW laser beam was focused by 100× objective at the Olympus BX41 confocal microscope, to a point of approximately 2 μm^2. The aperture diameter was set to 150 μm, and the 600 gr/mm grating was used. Accumulation time was 150 seconds with 4 repetititive scans.

Nickel mineralization in the Hatrurim Formation

Yakubovichite was discovered in the Hatrurim Formation – the world's largest pyrometamorphic complex whose outcrops are exposed in the area of 150×200 km^2 across the Dead Sea Transform fault system (e.g., Ben-Avraham et al. 2008), in Israel, Palestinian Authority and Jordan. Geological setting, stratigraphy and the origin of this complex, also known as the Mottled Zone, was reviewed in previous works (Gross 1977; Burg et al. 1992; Vapnik et al. 2007; Novikov et al. 2013; Abzalov et al. 2015). Pyrometamorphic lithologies were formed through the extensive high-temperature calcination and fusion of chalky-marly sedimentary sequences of late Cretaceous - early Paleogene age (e.g., Britvin et al. 2022b). Elevated Ni contents (up to hundreds ppm) were reported in these sediments both in Israel and Jordan (e.g., Issar et al. 1969; Ilani et al. 1985; Gilat 1994; Bogoch et al. 1999; Fleurance et al. 2013), but the mineralogical speciation of Ni was not investigated. The unique Ni-bearing phosphide mineralization, discovered in the Mottled Zone for the last decade, obviously originates from metamorphosed Ni-enriched sedimentary beds (Britvin et al. 2015, 2020c, 2022a). Besides phosphides, Ni in this rock complex tends to concentrate in oxide minerals.

Trevorite, $NiFe_2O_4$, a rare spinel-group mineral, was initially discovered in anomalous Ni oxide ore of the Bon Accord orebody, Kaapvaal craton, Barberton greenstone belt, South Africa (Walker 1923; De Waal 1972). Subsequently, it was reported in peridotites of the Mount Clifford deposit, Western Australia (Hudson and Travis 1981), pyroxenites of the Baikal rift zone, Russia (Muravyeva and Senin 1993), in the Mid-Ocean ridge basalt, Pacific Ocean (Pandey et al. 2008) and in impact melt veins of the Morokweng impact structure, South Africa (e.g., Koerbl et al. 1997). In the Hatrurim Formation, trevorite was briefly mentioned with no supplemental analytical data (Sharygin et al. 2013; Krzątała et al. 2020). We detected trevorite in phosphide-bearing assemblages of the Hatrurim Formation on both Israel and Jordan sides of the Dead Sea basin. In the Halamish wadi, Hatrurim basin, Israel, trevorite was found as an accessory mineral in diopside paralava, where it forms euhedral crystals up to 30 µm associated with keplerite $Ca_9Mg(Ca_{0.5}\square_{0.5})(PO_4)_7$ (Britvin et al. 2021b), hematite, and diopside (Fig. 1). In the type locality of yakubovichite – an abandoned phosphorite quarry in the Daba-Siwaqa complex, Transjordan Plateau, Jordan (31° 21' 52" N, 36° 10' 55" E), trevorite was found in clinopyroxene-plagioclase paralava containing phosphides - nickolayite, FeMoP (Murashko et al. 2022), and orishchinite, $(Ni,Fe,Mo)_2P$ (Britvin et al. 2022c). Representative chemical compositions of trevorite are provided in Table 1. The mineral

This is the peer-reviewed, final accepted version for American Mineralogist, published by the Mineralogical Society of America.
The published version is subject to change. Cite as Authors (Year) Title. American Mineralogist, in press.
DOI: https://doi.org/10.2138/am-2022-8800. http://www.minsocam.org/

has varying chemical composition, but the intragrain zoning has never been observed. An interesting feature of trevorite from the Hatrurim Formation is that it is completely devoid of Mg. It is noteworthy that, with NiO contents of 30 wt.%, this trevorite is the most Ni-rich variety of the mineral in nature (cf. Beckett-Brown and McDonald 2018).

Bunsenite, a naturally occurring NiO, was discovered at Johanngeorgenstadt, Erzgebirge, Saxony, Germany, within the specific mineral assemblages formed by the "dry oxidation" of Ni arsenide ores of the Ag–Bi–Co–Ni–U formation (Bergemann 1858; Roberts et al. 2001, 2004). Subsequently, the mineral was described in association with trevorite in the above-mentioned Bon-Accord orebody (De Waal 1972). Other reported occurrences (www.mindat.org, accessed August 2022) require additional confirmation. Bunsenite, like trevorite, was previously mentioned in the Hatrurim Formation (Khoury 2020), but without analytical data. We have found bunsenite in the phosphorite quarry in the Daba-Siwaqa complex, Jordan, where it occurs in phosphide-bearing clinopyroxene-plagioclase paralava. The mineral forms unusual amoeboid-shaped incrustations, surrounding microcavities within trevorite veinlets and rims, which are embedded into Ni-bearing hematite (Fig. 2). Bunsenite grains extracted from the paralava have a deep apple-green colour. Chemical composition of the mineral, along with composition of associated trevorite and hematite, is given in Table 1. Structural identity of bunsenite was confirmed with powder X-ray diffraction pattern, which contains the following lines [*d*(Å)(*I*)(*hkl*)]: 2.4135(75)(111), 2.0896(100)(200), 1.4774(30)(220), 1.2599(10)(311), 1.2064(6)(222), 1.0447(2)(400), 0.9588(2)(331). The refined *a* parameter value is 4.1793(2) Å, V = 72.995(4) Å^3.

Hematite–Eskolaite series Fe_2O_3 – Cr_2O_3. Nickeliferous members of the solid solution hematite-eskolaite are common in phosphide-phosphate-bearing assemblages, both in Israel and Jordan. They form granular aggregates composed of euhedral to platy crystals, disseminated within clinopyroxene-plagioclase paralavas (Fig. 1 and 2). Representative chemical compositions are presented in Table 1. The minerals contain up to 2 wt.% NiO. Their structural identity (hematite structural type) was confirmed by means of electron backscatter diffraction of representative grains.

Intermediate oxides of hematite-eskolaite series are known in nature and as synthetic compounds (e.g., Pérez-Cruz et al. 2015). The possibility of Ni incorporation into hematite was demonstrated on synthetic samples with up 2 wt.% Ni (Frierdich et al. 2011; Gadol et al. 2017). However, to the best of our knowledge, Ni contents in natural hematite are everywhere below detection limit of electron microprobe analysis. Therefore, nickeliferous hematite-eskolaite minerals from the Hatrurim Formation are likely the most Ni-rich varieties encountered in nature.

It is noteworthy that Ni-bearing oxides described above, Ni-phosphides and phosphates, including yakubovichite, are confined to the same type of rocks – diopside-clinopyroxene paralavas developed at the extent of the sedimentary beds of Cretaceous-Paleogene age. The possible sources of Ni in these rocks are discussed in this article.

Occurrence, appearance and physical properties of yakubovichite

Yakubovichite was discovered in paralavas (fused sedimentary rocks) exposed in the abandoned phosphorite quarry in the Daba-Siwaqa pyrometamorphic complex, Jizah District, Amman Governorate, Jordan (31° 21' 52'' N, 36° 10' 55'' E). The host paralava consists almost entirely of aggregates of long-prismatic colorless diopside crystals up to 1×5 mm in size, with rare anorthite, secondary calcite and hydrous Ca-silicates infilling the interstices between diopside crystals. Diopside has nearly ideal $CaMgSi_2O_6$ composition, with Fe and Al contents below 0.05 wt.%. The most common accessory mineral is microcrystalline hematite. Phosphate-phosphide assemblages form irregularly shaped centimeter-sized nests in paralava, and consist of hematite, crocobelonite $CaFe_2^{3+}(PO_4)_2O$ (IMA 2020-005), Ni-phosphides – negevite NiP_2, halamishite Ni_5P_4, and transjordanite Ni_2P (Britvin et al. 2020a,b,c), and Fe-Ni bearing phosphates (Fig. 3).

Yakubovichite forms polycrystalline segregations up to 0.2 mm in size composed of equant crystal grains, in association with crocobelonite, hematite, other phosphates and phosphides (Fig. 3). The mineral has a deep yellow to lemon-yellow colour (typical of anhydrous Ni-bearing phosphates) and yellowish-white strike. It is transparent to translucent with vitreous luster. Yakubovichite has no cleavage; Mohs hardness = 4. Density, calculated based on the empirical formula and unit-cell parameters refined from X-ray single-crystal data, is 3.657 g cm^{-3}. In thin sections and in immersion liquids in transmitted light, yakubovichite has pale-yellow to lemon-yellow colour, depending on grain thickness. It is non-pleochroic. In crossed polars, yakubovichite grains exhibit undulatory extinction that prevents from estimations of 2V value. Biaxial (−), $2V_{calc}$ = 38°, α = 1.725(3), β = 1.765(3), γ = 1.775(3). The Gladstone-Dale compatibility index (Mandarino 1976), 1-(K_P/K_C) = 0.011 (superior).

Since the approval of yakubovichite by CNMNC, IMA, yakubovichite was also recognized in phosphide-phosphate assemblages found in the Halamish Wadi, Hatrurim Basin, Negev desert, Israel (detailed description of locality is given in: Britvin et al. 2015, 2022b). The association of yakubovichite from the Halamish Wadi is very similar to that of the holotype material from Jordan, but the mineral grains are rather small (less than 10 μm). The structural identity of the mineral from the Halamish Wadi was confirmed using electron backscatter diffraction method.

Chemical composition

Electron microprobe data for yakubovichite are summarized in Table 2. It can be seen that chemical composition of the mineral from Jordan (the holotype) is very similar to that of yakubovichite from Israel. All iron was assumed to be Fe^{3+}, according to the results of bond-valence calculations for holotype yakubovichite (bond-valence sum for Fe site is 3.07 valence units, Table 3). Element grouping in the empirical formula of the mineral was performed according to the stoichiometry of $CaNi_2Fe^{3+}(PO_4)_3$ – the synthetic analogue of yakubovichite (Ouaatta et al. 2017). The empirical formula of holotype yakubovichite based on 12 oxygen atoms per formula unit is $(Ca_{0.55}Na_{0.29}K_{0.18}Ba_{0.04}Sr_{0.02})_{1.08}(Ni_{1.39}Mg_{0.26}Fe^{3+}_{0.24}V^{3+}_{0.03}Cu_{0.01}Cr_{0.01})_{1.94}(Fe^{3+}_{0.90}Al_{0.10})_{1.00}P_{3.02}O_{12}$. The formula of the mineral from Israel is: $(Ca_{0.63}Na_{0.23}K_{0.11}Ba_{0.08}Sr_{0.02})_{1.07}(Ni_{1.30}Mg_{0.41}Fe^{3+}_{0.16}V^{3+}_{0.06}Cu_{0.01}Cr_{0.01})_{1.95}(Fe^{3+}_{0.94}Al_{0.06})_{1.00}(P_{3.00}Si_{0.02})_{3.02}O_{12}$. The ideal formula of yakubovichite is $CaNi_2Fe^{3+}(PO_4)_3$.

Crystal structure and powder X-ray diffraction

Yakubovichite is the first mineral that crystallizes in the α-$CrPO_4$ structure type (Attfield et al. 1988). The crystal structure was solved and refined on the holotype material from the Jordan locality. It represents a framework built up of corner- end edge-sharing [MO_6] octahedra, and [PO_4] tetrahedra (Fig. 4). The two kinds of channels penetrate the structure along the *a*- and *b*-axes, respectively. The channels are filled with alkali-earth and alkali cations (the eight-fold coordinated *A* (4*e*) site), whereas in α-$CrPO_4$ the corresponding channels are vacant. The octahedrally coordinated *M*1 (4*a*) site is predominantly populated by Fe^{3+}, whereas the *M*2 (8*g*) site is Ni-dominant (Table 3). The bond-valence sums for corresponding metal and phosphorus sites are well consistent with formal cation charges calculated based on the empirical formula (Table 3). There is a direct synthetic analogue of yakubovichite, $CaNi_2Fe^{3+}(PO_4)_3$ (Ouaatta et al. 2017), and its Sr counterpart, $SrNi_2Fe^{3+}(PO_4)_3$ (Ouaatta et al. 2015) (Table 4). The powder X-ray diffraction pattern of yakubovichite is given in Table 5.

Raman spectroscopy

The Raman spectrum of yakubovichite is consistent with its chemical composition and structure, as an anhydrous orthophosphate (Nakamoto 2008). The fingerprint region (Fig. 5a) contains the following bands (cm^{-1}): 105, 142, 173, 187, 198, 228, 259, 290, 324, 378 ([MO_6] and lattice modes); 416, 471, 495 [ν_2 (symmetric bending (PO_4) vibrations]; 542, 560, 590, 629, 664, 742 [ν_4 (asymmetric bending (PO_4) modes]; 936 [ν_1 (symmetric stretching P-O)]; 1040, 1054, 1100, 1141 [ν_3 (asymmetric stretching P-O)]. From the chemical point of view, the absence of bands in the O–H stretching region (3800–3000 cm^{-1}) and bending modes corresponding to molecular H_2O (1630–1670 cm^{-1}) (Fig. 5b) evidences that the mineral does not contain water, that corroborates with electron microprobe analyses, crystal structure and optical data.

Discussion: structural links between yakubovichite, galileiite and xenophyllite

The possible structural analogues of yakubovichite are the two meteoritic minerals, galileiite (Olsen and Steele 1997) and xenophyllite (Britvin et al. 2020d). Unfortunately, the crystal structures of both species were not determined; therefore, one can only rely on the chemical composition, X-ray powder diffraction data and unit-cell parameters (Table 4). Galileiite was described as a new mineral from several IIIAB group iron meteorites with a proposed formula $NaFe_4^{2+}(PO_4)_3$ (Olsen and Steele 1997; Olsen et al. 1999), and was reported from other iron and chondritic meteorites (Chen and Xie 1996; Sugiura and Hoshino 2003; Xie et al. 2014; Sharygin et al. 2016). Based on the X-ray powder diffraction pattern, the mineral was ascribed to the fillowite group (Olsen and Steele (1997). However, the authors have noted that the pattern indexing in the fillowite unit cell was not entirely satisfactory, and the assertion of galileiite as a mineral belonging to the fillowite group "is yet to be demonstrated" (Olsen and Steele 1997). It should be noted that such a demonstration was not yet completed; therefore, the assignment of galileiite to either structural type (or mineral group) is a debatable question, since the synthetic chemical analogue of galileiite, $Na_{1.1}Fe_4(PO_4)_3$ (Zhang et al. 2018) adopts a distorted α-$CrPO_4$ structure (Table 4).

Xenophyllite, ideally $Na_4Fe_7(PO_4)_6$, is another meteoritic phosphate discovered in the IIIAB iron meteorite, Augustinovka (Britvin et al. 2020d). The chemical formula of the mineral, its space group and unit-cell parameters are consistent with those of synthetic phosphates $ANa_3M_7(PO_4)_6$ where A = K, Rb, Cs; M = Fe^{2+}, Mg, Mn, Zn (Yakubovich et al. 1996; Queen et al. 2007; Guo et al. 2014; Ben Hamed et al. 2017). The direct chemical analogue of xenophyllite was reported by Pu et al. (2019). All these compounds represent variations of the α-$CrPO_4$ structure type (Britvin et al. 2020d). Moreover, there is a continuous series of solid solutions between xenophyllite, $Na_4Fe_7(PO_4)_6$, and the α-$CrPO_4$-related mineral with the chemical formula of $Na_2Fe_8(PO_4)_6$ – i.e., the formula of galileiite. The possible structural relationships between xenophyllite, galileiite and α-$CrPO_4$ were discussed by Britvin et al. (2020d).

Formation conditions of yakubovichite

Pyrometamorphic processes that dominated during the formation of yakubovichite-bearing assemblages, imply the high-temperature oxidative environment, near-atmospheric pressure, and the lack of water in the system. The synthetic analogue of yakubovichite, $CaNi_2Fe^{3+}(PO_4)_3$, was prepared by crystallization from dry phosphate melt fused at 1160 °C (Ouatta et al. 2017). This temperature looks reasonable for the conditions that expectedly occurred during the setup of the Hatrurim Formation (Gross 1977; Burg et al. 1992; Vapnik et al. 2007). The association with Ni-phosphides – negevite NiP_2, halamishite Ni_5P_4 and transjordanite Ni_2P – evidences that yakubovichite might be formed as a result of pyrolytic oxidation (dry roasting) of these phosphides. The latter process could be accompanied by side reactions with Ca-bearing minerals – calcite, lime or fluorapatite, – which served as a source of Ca. In this respect, formation conditions of yakubovichite might resemble those that likely occurred during the formation of anhydrous Ni-arsenates in the oxidized ores of the Erzgebirge mining district (Roberts et al. 2001, 2004; Kampf et al. 2020). The similar (but less hot) conditions occur within oxidizing-type arsenate fumaroles of the Tolbachik volcano, Kamchatka Peninsula, Russia (Pekov et al. 2018).

Geological implications

As it was pointed out in the introduction, Ni on Earth is an element characteristic of ultramafic complexes and in particular, sulfide ores associated with these formations. In addition, Ni is a mandatory constituent of Fe-Ni metal in iron and stony-iron meteorites, which are accepted to represent the inner parts of small planetary bodies (planetesimals) (Buchwald 1975). These geochemical and cosmochemical reservoirs of Ni can sometimes be interconnected. As an example, there is a consensus that the Sudbury structure in Canada, which hosts the world largest Fe-Ni sulfide deposits, is of meteoroid impact origin (Grieve and Therriault 2000). The anomalous Bon-Accord orebody, known for the extreme Ni enrichment, is considered by several researchers as a metamorphically assimilated iron meteorite (O'Driscoll et al. 2014). Yakubovichite, with 20 wt.% NiO in the chemical composition, comprises the extremely Ni-rich phosphate assemblages whose origin has no obvious links to the above mentioned Ni sources. The same is valid for other Ni-rich minerals in the Hatrurim Formation – Ni-phosphides, bunsenite NiO, trevorite $FeNi_2O_4$ or nickeliferous members of the hematite-eskolaite series, Fe_2O_3-Cr_2O_3. There are no ultrabasic complexes in the territory of Southern Levant. Mineralogical records of a possible high-pressure (impact) event, which could trigger pyrometamorphic processes in the Dead Sea Transform fault system, were reported (Britvin et al. 2021c, 2022d), but there are no geological evidences that could support mineralogical data.

The elevated Ni contents in the Cretaceous-Paleogene sediments – the protoliths of pyrometamorphic lithologies – were ascribed to hydrothermal activity related to the development of the Dead Sea Transform fault system (Fleurance et al. 2013). In this respect, we would like to focus on the fact that pyrometamorphic rocks of the Hatrurim Formation were developed at the expense of the sediments belonging to a Cretaceous-Paleogene (Cretaceous-Tertiary) boundary (Fig. 6). On the geological timescale, this boundary, ~66 Ma age, marks the period of mass extinction of living species, and is commonly associated with the catastrophic Earth-meteorite collision occurred at the Chicxulub impact crater (Alvarez et al. 1980; Smit 1999; Grieve and Therriault 2000). The elevated Ni contents in the Cretaceous-Paleogene boundary layer are connected with the presence of impact spherules, which contain abundant Ni-bearing spinels enriched in trevorite component (Kyte and Smit 1986; Robin et al. 1992). The corresponding mineralogical studies of the Cretaceous-Paleogene boundary layer in the Southern Levant might shed light on the origin of anomalous Ni mineralogy in pyrometamorphic lithologies of the Hatrurim Formation.

Acknowledgements

The authors are grateful to the referees, Robert Hazen and an anonymous one, for valuable comments and suggestions, and to Associate Editor, Fabrizio Nestola, for editorial handling of the manuscript. We are indebted to The study was completed under financial support of the Russian Science Foundation, grant 18-17-00079. We sincerely thank the Centre for X-ray diffraction studies, Geomodel Resource Centre, Centre for Microscopy and Microanalysis, Centre for Optical and Laser Materials Research and Centre for Diagnostics of Functional Materials for Medicine, Pharmacology and Nanoelectronics of St. Petersburg State University for the access to instrumental and computational resources.

References

Abzalov, M.Z., Heyden, A., van der, Saymeh, A., and Abuqudaira, M. (2015) Geology and metallogeny of Jordanian uranium deposits. Applied Earth Science, 124, 63–77.

Alvarez, L.W., Alvarez, W., Asaro, F., and Michel, H.V. (1980) Extraterrestrial cause for the Cretaceous-Tertiary extinction. Science, 208, 1095–1108.

Attfield, J.P., Cheetham, A.K., Cox, D.E., and Sleight, A.W. (1988) Synchrotron X-ray and neutron powder diffraction studies of the structure of α-$CrPO_4$. Journal of Applied Crystallography, 21, 452–457.

Barnes, S.J., Malitch, K.N., and Yudovskaya, M.A. (2020) Introduction to the special issue on the Norilsk-Talnakh Ni-Cu-platinum group element deposits. Economic Geology, 115, 1157–1172.

Begg, G.C., Hronsky, J.M.A., Arndt, N.T., Griffin, W.L., OReilly, S.Y., and Hayward, N. (2010) Lithospheric, cratonic and geodynamic setting of Ni-Cu-PGE sulfide deposits. Economic Geology 105, 1057–1070.

Beckett-Brown, C.E., and McDonald, A.M. (2018) The crystal-chemistry of Ni-bearing spinel-group minerals: Chemical, geological and exploration implications. Canadian Mineralogist 56, 77–94.

Ben-Avraham, Z., Garfunkel, Z., and Lazar, M. (2008) Geology and evolution of the Southern Dead Sea Fault with emphasis on subsurface structure. Annual Review of Earth and Planetary Sciences, 36, 357–387.

Ben Hamed, T., Boukhris, A., Badri, A., and Ben Amara, M. (2017) Synthesis and crystal structure of a new magnesium phosphate $Na_3RbMg_7(PO_4)_6$. Acta Crystallographica, E73, 817−812.

Bergemann, C. (1858) Ueber einige Nickelerze. Journal für Praktische Chemie, 75, 239–244.

Bogoch, R., Gilat, A., Yoffe, O., and Ehrlich, S. (1999). Rare earth trace element distributions in the Mottled Zone complex, Israel. Israel Journal of Earth Sciences, 48, 225–234.

Brese, N.E., and O'Keeffe, M. (1991) Bond-valence parameters for solids. Acta Crystallographica, B47, 192–197.

Britvin, S.N., Murashko, M.N., Vapnik, Ye., Polekhovsky, Yu.S., and Krivovichev, S.V. (2015) Earth's phosphides in Levant and insights into the source of Archaean prebiotc phosphorus. Scientific Reports, 5, 8355.

Britvin, S.N., Dolivo-Dobrovolsky, D.V., and Krzhizhanovskaya, M.G. (2017) Software for processing the X-ray powder diffraction data obtained from the curved image plate detector of Rigaku RAXIS Rapid II diffractometer. Zapiski Rossiiskogo Mineralogicheskogo Obshchestva, 146(3), 104–107 (in Russian).

Britvin, S.N., Murashko, M.N., Vapnik, Ye., Polekhovsky, Yu.S., Krivovichev, S.V., Krzhizhanovskaya, M.G., Vereshchagin, O.S., Shilovskikh, V.V., and Vlasenko, N.S. (2020a) Transjordanite, Ni_2P, a new terrestrial and meteoritic phosphide, and natural solid solutions barringerite–transjordanite (hexagonal Fe_2P–Ni_2P). American Mineralogist, 105, 428–436.

Britvin, S.N., Murashko, M.N., Vapnik, Ye., Polekhovsky, Yu.S., Krivovichev, S.V., Vereshchagin, O.S., Shilovskikh, V.V., Vlasenko, N.S., and Krzhizhanovskaya, M.G. (2020b) Halamishite, Ni_5P_4, a new terrestrial phosphide in the Ni–P system. Physics and Chemistry of Minerals, 2020, 3.

Britvin, S.N., Murashko, M.N., Vapnik, Ye., Polekhovsky, Yu.S., Krivovichev, S.V., Vereshchagin, O.S., Shilovskikh, V.V., and Krzhizhanovskaya, M.G. (2020c) Negevite, the pyrite-type NiP_2, a new terrestrial phosphide. American Mineralogist, 105, 422–427.

Britvin, S.N., Krivovichev, S.V., Obolonskaya, E.V., Vlasenko, N.S., Bocharov, V.N., and Bryukhanova, V.V. (2020d) Xenophyllite, $Na_4Fe_7(PO_4)_6$, an exotic meteoritic phosphate: new mineral description, Na-ions mobility and electrochemical implications. Minerals, 10, 300.

Britvin, S.N., Murashko, M.N., Vapnik, Ye., Vlasenko, N.S., Krzhizhanovskaya, M.G., Vereshchagin, O.S., Bocharov, V.N., and Lozhkin, M.S. (2021a) Cyclophosphates, a new class of native phosphorus compounds, and some insights into prebiotic phosphorylation on early Earth. Geology, 49, 382–386.

Britvin, S.N., Galuskina, I.O., Vlasenko, N.S., Vereshchagin, O.S., Bocharov, V.N., Krzhizhanovskaya, M.G., Shilovskikh, V.V., Galuskin, E.V., Vapnik, Ye., and Obolonskaya, E.V. (2021b) Keplerite, $Ca_9(Ca_{0.5}\square_{0.5})Mg(PO_4)_7$, a new meteoritic and terrestrial phosphate isomorphous with merrillite, $Ca_9NaMg(PO_4)_7$. American Mineralogist, 106, 1917–1927.

Britvin, S.N., Vereshchagin, O.S., Shilovskikh, V.V., Krzhizhanovskaya, M.G., Gorelova, L.A., Vlasenko, N.S., Pakhomova, A.S., Zaitsev, A.N., Zolotarev, A.A., Bykov, M., Lozhkin, M.S., and Nestola, F. (2021c) Discovery of terrestrial allabogdanite $(Fe,Ni)_2P$, and the effect of Ni and Mo substitution on the barringerite-allabogdanite high-pressure transition. American Mineralogist, 106, 944–952.

Britvin, S.N., Murashko, M.N., Krzhizhanovskaya, M.G., Vereshchagin, O.S., Vapnik, Ye., Shilovskikh, V.V., Lozhkin, M.S., and Obolonskaya, E.V. (2022a) Nazarovite, $Ni_{12}P_5$, a new terrestrial and meteoritic mineral structurally related to nickelphosphide, Ni_3P. American Mineralogist, doi:10.2138/am-2022-8219.

Britvin, S.N., Murashko, M.N., Vereshchagin, O.S., Vapnik, Ye., Shilovskikh, V.V., Vlasenko, N.S., and Permyakov, V.V. (2022b) Expanding the speciation of terrestrial molybdenum: discovery of polekhovskyite, $MoNiP_2$, and insights into the sources of Mo-phosphides in the Dead Sea Transform area, American Mineralogist, doi:10.2138/am-2022-8261.

Britvin, S.N., Murashko, M.N., Vapnik, Y., Zaitsev, A.N., Shilovskikh, V.V., Vasiliev, E.A., Krzhizhanovskaya, M.G., and Vlasenko, N.S. (2022c) Orishchinite, a new terrestrial phosphide, the Ni-dominant analogue of allabogdanite. Mineralogy and Petrology, doi:10.1007/s00710-022-00787-x

Britvin, S.N., Vlasenko, N.S., Aslandukov, A., Aslandukova, A., Dubrovinsky, L., Gorelova, L.A., Krzhizhanovskaya, M.G., Vereshchagin, O.S., Bocharov, V.N., Shelukhina, Yu.S., Lozhkin, M.S., Zaitsev, A.N., and Nestola, F. (2022d) Natural cubic perovskite, Ca(Ti,Si,Cr)$O_{3-\delta}$, a versatile potential host for rock-forming and less common elements up to Earth's mantle pressure. American Mineralogist, doi: 10.2138/am-2022-8186

Buchwald, V.F. (1975) Handbook of iron meteorites, 3 vols. University of California Press, Berkeley.

Buchwald, V.F. (1990) A new mineral, arupite, $Ni_3(PO_4)_2 \cdot 8H_2O$, the nickel analogue of vivianite. Neues Jahrbuch für Mineralogie, Monatshefte, 1990, 76–80.

Burg, A., Starinsky, A., Bartov, Y., and Kolodny, Y. (1992) Geology of the Hatrurim Formation ("Mottled Zone") in the Hatrurim basin. Israel Journal of Earth Sciences, 40, 107–124.

Chen, M., and Xie, X. (1996) Na behavior in shock-induced melt phase of the Yanzhuang (H6) chondrite. European Journal of Mineralogy, 8, 325–333.

De Waal, S.A. (1972) Nickel minerals from Barberton, South Africa: V. Trevorite, redescribed. American Mineralogist, 57, 1524–1527.

Dolomanov, O.V., Bourhis, L.J., Gildea, R.J., Howard, J.A., and Puschmann, H. (2009) OLEX2: a complete structure solution, refinement and analysis program, Journal of Applied Crystallography, 42, 339–341.

Fleurance, S., Cuney, M., Malartre, M., and Reyx, J. (2013) Origin of the extreme polymetallic enrichment (Cd, Cr, Mo, Ni, U, V, Zn) of the Late Cretaceous–Early Tertiary Belqa Group, central Jordan. Palaeogeography, Palaeoclimatology, Palaeoecology, 369, 201–219.

Frierdich, A. J., Luo, Y., and Catalano, J. G. (2011) Trace element cycling through iron oxide minerals during redox-driven dynamic recrystallization. Geology, 39, 1083−1086.

Gadol, H. J., Flynn, E. D., and Catalano, J. G. (2017) Oxalate-promoted trace metal release from crystalline iron oxides under aerobic conditions. Environmental Science & Technology Letters, 4, 311−315.

Gilat, A. (1994) Tectonic and associated mineralization activity, Southern Judea, Israel. Geological Survey of Israel, Report GSI/19/94, Jerusalem, 322 p.

Grieve, R., and Therriault, A. (2000) Vredefort, Sudbury, Chicxulub: Three of a Kind? Annual Reviews in Earth and Planetary Science, 28, 305–338.

Gross, S. (1977) The mineralogy of the Hatrurim Formation, Israel. Geological Survey of Israel Bulletin, 70, 1–80.

Guilcher, M., Schmaucks, A., Krause, J., Markl, G., Gutzmer, J., and Burisch, M. (2021) Vertical zoning in hydrothermal U-Bi-Co-Ni-As-Ag systems - a case study from the Annaberg-Buchholz district, Erzgebirge (Germany). Economic Geology, 116, 1893–1915.

Guo, W., He, Z., Zhang, S., Yang, M., Tang, Y., and Cheng, W. (2014) $KNa_3Mn_7(PO_4)_6$: 2D spin-frustrated magnetic material with a diamond-like chain structure. RSC Advances, 4, 21559−21562.

Hawley, J.E. (1962) The Sudbury ores: their mineralogy and origin. Canadian Mineralogist, 7, 1–202.

Hoatson, D.M., Jaireth, S., and Jaques, A.L. (2006) Nickel sulfide deposits in Australia: Characteristics, resources, and potential. Ore Geology Reviews, 29, 177–241.

Hudson, D.R., and Travis, G.A. (1981) A native nickel-heazlewoodite-ferroan trevorite assemblage from Mount Clifford, western Australia. Economic Geology, 76, 1686–1697.

Ilani, S., Kronfeld, J., and Flexer, A. (1985) Iron-rich veins related to structural lineaments, and the search for base metals in Israel. Journal of Geochemical Exploration, 24, 197–206.

Issar, A., Eckstein, Y., and Bogoch, R. (1969) A possible thermal spring deposit in the Arad area, Israel. Israel Journal of Earth Sciences, 18, 17–20.

Kampf, A.R., Nash, B.P., Plášil, J., Smith, J.B., and Feinglos, M.N. (2020) Niasite and johanngeorgenstadtite, $Ni^{2+}_{4.5}(AsO_4)_3$ dimorphs from Johanngeorgenstadt, Germany. European Journal of Mineralogy, 32, 373–385.

Khoury, H.N. (2020) High- and low-temperature mineral phases from the pyrometamorphic rocks, Jordan. Arabian Journal of Geosciences, 13, 734.

Kyte, F.T., and Smit, J. (1986) Regional variations in spinel compositions: An important key to the Cretaceous/Tertiary event. Geology, 14, 485–487.

Koeberl, C., Armstrong, R.A., and Reimold, W.U. (1997) Morokweng, South Africa: A large impact structure of Jurassic-Cretaceous boundary age. Geology, 25, 731–734.

Krzątała, A., Krüger, B., Galuskina, I., Vapnik, Y., and Galuskin, E. (2020) Walstromite, $BaCa_2(Si_3O_9)$, from rankinite paralava within gehlenite hornfels of the Hatrurim Basin, Negev Desert, Israel. Minerals, 10, 407.

Muravyeva, N.S., and Senin, V.G. (1993) Trevorite in pyroxenite nodules from the Tokinsky Stanovik Mountains (ENE prolongation of Baikal rift zone). Mineralogical Magazine, 57, 171–173.

Mandarino, J.A. (1976) The Gladstone-Dale relationship. Part I: Derivation of new constants. Canadian Mineralogist, 14, 498–502.

Meyer, C. (1968) Ore Deposits. Nickel. International Geological Review – Book Series, 10, 72–82.

Murashko, M.N., Britvin, S.N., Vapnik, Y., Polekhovsky, Y.S., Shilovskikh, V.V., Zaitsev, A.N., Vereshchagin, O.S. (2022) Nickolayite, FeMoP, a new natural molybdenum phosphide. Mineralogical Magazine, doi doi:10.1180/mgm.2022.52

Nakamoto K. (2008) Infrared and Raman Spectra of Inorganic and Coordination Compounds, Theory and Applications in Inorganic Chemistry. John Wiley and Sons, New York.

Novikov, I., Vapnik, Ye., and Safonova, I. (2013) Mud volcano origin of the Mottled Zone, Southern Levant. Geoscience Frontiers, 4, 597–619.

O'Driscoll, B., Clay, P.L., Cawthorn, R.G., Lenaz, D., Adetunji, J., and Kronz, A. (2014) Trevorite: Ni-rich spinel formed by metasomatism and desulfurization processes at Bon Accord, South Africa? Mineralogical Magazine, 78, 145–163.

Olsen, E. J., and Steele, I.M. (1997) Galileiite: A new meteoritic phosphate mineral. Meteoritics & Planetary Science, 32, A155–A156.

Olsen, E.J., Kracher, A., Davis, A.M., Steele, I.A., Hutcheon, I.D., and Bunch, T.E. (1999) The phosphates of IIIAB iron meteorites. Meteoritics and Planetary Science, 34, 285–300.

Ondruš, P., Veselovský, F., Gabašová, A., Hloušek, J., and Šrein, V. (2003) Geology and hydrothermal vein system of the Jáchymov (Joachimsthal) ore district. Journal of the Czech Geological Society, 48, 3–18.

Ouaatta, S., Assani, A., Saadi, M., and El Ammari, L. (2015) Crystal structure of strontium dinickel iron orthophosphate. Acta Crystallographica, E71, 1255–1258.

Ouaatta, S., Assani, A., Saadi, M., and El Ammari, L. (2017) Crystal structure of calcium dinickel(II) iron(III) tris(orthophosphate): $CaNi_2Fe(PO_4)_3$. Acta Crystallographica, E73, 893–895.

Pandey, S.K., Shrivastava, J.P., and Roonwal, G.S. (2008) Occurrence of ferroan trevorite within olivine megacrysts of the MORB from the Southern East Pacific Rise. Current Science, 95, 1468–1473.

Pekov, I.V., Koshlyakova, N.N., Zubkova, N.V., Lykova, I.S., Britvin, S.N., Yapaskurt, V.O., Agakhanov, A.A., Shchipalkina, N.V., Turchkova, A.G., and Sidorov, E.G. (2018) Fumarolic arsenates - a special type of arsenic mineralization. European Journal of Mineralogy, 30, 305–322.

Pérez-Cruz, M.A., Elizalde-González, M.P., Escudero, R.B., Bernès, S., Silva-González, R., and Reyes-Ortega, Y. (2015) At last! The single-crystal X-ray structure of a naturally occurring sample of the ilmenite-type oxide $FeCrO_3$. Acta Crystallographica, B71, 555–561.

Petruk, W. (1971): Mineralogical characteristics of the deposits and textures of the ore minerals. In The Silver-Arsenide Deposits of the Cobalt-Gowganda Region, Ontario. Canadian Mineralogist, 11, 108–139.

Pu, X., Rong, C., Tang, S., Wang, H., Cao, S., Ding, Y., Cao Y., and Chen, Z. (2019) Zero-strain $Na_4Fe_7(PO_4)_6$ as a novel cathode material for sodium–ion batteries. Chemical Communications, 55, 9043–9046.

Queen, W.L., Hwu, S.-J., and Wang, L. (2007) A Low-Dimensional Iron(II) Phosphate Exhibiting Field-Dependent Magnetization Steps. Angewandte Chemie International Edition, 46, 5344−5347.

Roberts, A.C., Burns, P.C., Gault, R.A., Criddle, A.J., Feinglos, M.N., and Stirling, J.A.R. (2001) Paganoite, $NiBiAsO_5$, a new mineral from Johanngeorgenstadt, Saxony, Germany: description and crystal structure. European Journal of Mineralogy, 13, 167–175.

Roberts, A.C., Burns, P.C., Gault, R.A., Criddle, A.J., and Feinglos, M.N. (2004) Petewilliamsite, $(Ni,Co)_{30}(As_2O_7)_{15}$, a new mineral from Johanngeorgenstadt, Saxony, Germany: description and crystal structure. Mineralogical Magazine, 68, 231–240.

Robin, E., Bonté, P., Froget, L., Jéhanno, C., and Rocchia, R. (1992) Formation of spinels in cosmic objects during atmospheric entry: A clue to the Cretaceous-Tertiary boundary event. Earth and Planetary Science Letters, 108, 181–190.

Sharygin, V.V., Lazic, B., Armbruster, T.M., Murashko, M.N., Wirth, R., Galuskina, I.O., Galuskin, E.V., Vapnik, Y., Britvin, S.N., and Logvinova, A.M. (2013): Shulamitite, $Ca_3TiFe^{3+}AlO_8$ - a new perovskite-related mineral from Hatrurim Basin, Israel. European Journal of Mineralogy 25, 97–111.

Sharygin, V.V., Karmanov, N.S., and Podgornykh, N.M. (2016) Na-Fe-phosphate globules in impact metal-troilite associations of Chelyabinsk meteorite. Proceeding of 79th Annual Meeting of Meteoritic Society, 2016, abstract 6052.

Sheldrick, G.M. (2015) Crystal structure refinement with SHELXL. Acta Crystallographica, C71, 3–8.

Smit, J. (1999) The Global Stratigraphy of the Cretaceous-Tertiary Boundary Impact Ejecta. Annual Review of Earth and Planetary Science, 27, 75–113.

Sugiura, N., and Hoshino, H. (2003) Mn–Cr chronology of five IIIAB iron meteorites. Meteoritics & Planetary Science, 38, 117–143.

Thorne, R.L., Roberts, S., and Herrington, R. (2012) Climate change and the formation of nickel laterite deposits. Geology, 40, 331–334.

Vapnik, Ye., Sharygin, V., Sokol, E., and Shagam, R. (2007) Paralavas in a combustion metamorphic complex, Hatrurim Basin, Israel. GSA Reviews in Engineering Geology, 18, 33–153.

Walker, T.L. (1923) Trevorite, a distinct mineral species. Contributions to Canadian Mineralogy, University of Toronto Studies, 16, 53–54.

White, J.S., Henderson, E.P., and Mason, B. (1967) Secondary minerals produced by weathering of the Wolf Creek meteorite. American Mineralogist, 52, 1190–1197.

Xie, X., Chen, M., Zhai, S., and Wang, F. (2014) Eutectic metal + troilite + Fe-Mn-Na phosphate + Al-free chromite assemblage in shock-produced chondritic melt of the Yanzhuang chondrite. Meteoritics & Planetary Science, 49, 2290–2304.

Yakubovich, O.V., Mel'nikov, O.K., Urusov, V.S., Massa, V., and Vochadlo, S. (1996) Crystal structure of a new orthophosphate $CsNa_3Zn_7(PO_4)_6$. Doklady Akademii Nauk SSSR, 348, 755−758.

Yakubovich, O.V., Shvanskaya, L.V., Bolotina, N.B., Ivanova, A.G., Kiriukhina, G.V., Dovgaliuk, I.N., Volkov, A.S., Dimitrova, O.V., and Vasiliev, A.N. (2021) An orthorhombic modification of $KCoPO_4$ stabilized under hydrothermal conditions: Crystal chemistry and magnetic behavior. Inorganic Chemistry, 60, 9461–9470.

Zhang, H., Zhao, Y., Wen, M., Dong, Y., Fan, Q., Kuang, Q., Liu, H., and Lian, X. (2018) A new sodium ferrous orthophosphate $Na_xFe_4(PO_4)_3$ as anode materials for sodium-ion batteries. Journal of Materials Science, 53, 8385–8397.

List of figure captions

Figure 1. Trevorite crystal in diopside paralava. Halamish Wadi, Hatrurim Basin, Negev desert, Israel. SEM BSE image. Abbreviations: Trv – trevorite; Hm – hematite; Di – diopside; Kpl – keplerite $Ca_9Mg(Ca_{0.5}\square_{0.5})(PO_4)_7$

Figure 2. Bunsenite, NiO, in clinopyroxene-plagioclase paralava. Daba-Siwaqa complex, Transjordan plateau, Jordan. (a) Bunsenite segregations (yellow) within trevorite veinlets (green) that encrust the microcracks in nickeliferous hematite (blue). False colour phase distribution map superimposed onto SEM BSE image. (b) The enlarged detail of the above picture, SEM BSE image. Abbreviations: Bse – bunsenite; Trv – trevorite; Hem – hematite.

Figure 3. Yakubovichite and associated minerals. Daba-Siwaqa complex, Transjordan plateau, Jordan (the type locality). (a) Yellow yakubovichite grain intergrown with brown crystals of moabite $NiFe^{3+}(PO_4)O$, brownish-red crocobelonite $CaFe_2^{3+}(PO_4)_2O$ and white diopside-anorthite aggregate. (b) Yellow yakubovichite grain intergrown with red crocobelonite, black areas composed of hematite and Ni-phosphides, and colorless diopside. Polished thin section, transmitted light. Legend: 1 – yakubovichite; 2 – moabite; 3 – crocobelonite; 4 – diopside and anorthite; 5 – hematite and Ni-phosphides.

Figure 4. Crystal structure of yakubovichite (α-$CrPO_4$ structure type). A three-dimensional framework consisting of corner- and edge-sharing [MO_6] octahedra and [PO_4] tetrahedra. The framework is penetrated by the two systems of channels: (a) the channels propagated along the *a*-axis and (b) those propagated along the *b*-axis. Alkali earth and alkali cations (not shown for clarity) reside in the channels. Blue tetrahedra, [PO_4]; yellow octahedra, [$M1O_6$]; green octahedra, [$M2O_6$].

Figure 5. Raman spectrum of yakubovichite. (a) The fingerprint region. (b) Region 1350-3800 cm^{-1}. The intensity scale in (a) and (b) is the same.

Figure 6. Stratigraphic position of pyrometamorphic lithologies of the Hatrurim Basin, Israel, and the coincident lithologies of the Daba-Siwaqa complex, Jordan, in the Late Cretaceous–Paleogene sequence of the Southern Levant. The stratigraphic equivalents of the Mottled Zone are highlighted by brown color. The Cretaceous-Paleogene boundary (~66 Ma) is marked by the red line. Redrawn based on the data of Britvin et al. (2021c).

This is the peer-reviewed, final accepted version for American Mineralogist, published by the Mineralogical Society of America.
The published version is subject to change. Cite as Authors (Year) Title. American Mineralogist, in press.
DOI: https://doi.org/10.2138/am-2022-8800. http://www.minsocam.org/

Table 1. Chemical composition of Ni-bearing oxides (wt.%) from the Hatrurim Formation [a]

Mineral	Trevorite				Bunsenite		Eskolaite	Hematite		
Locality	HB [b]	DS [b]	HB	DS	DS		DS	HB	DS	DS
Notes	Fig. 1			Fig. 2	Fig. 2					Fig. 2
NiO	29.93	30.15	29.23	29.24	89.73	90.11	1.83	1.25	2.38	1.73
CoO	0.53							0.23		
FeO					6.85	8.91				
CaO	0.41		0.35	0.48			0.51	0.40		0.57
CuO	1.36	1.64	1.18					0.17		
Al_2O_3	1.00	13.07	0.96	0.90	3.16	1.25	3.07			2.81
V_2O_3							2.59	0.69		
Cr_2O_3	1.60		2.75				55.42	0.34		2.36
Fe_2O_3	65.80	56.19	65.37	70.34			35.45	96.35	97.94	90.53
TiO_2							1.60	1.15		1.85
SiO_2					0.37	0.15				1.12
Total	100.63	101.05	99.84	100.96	100.11	100.42	100.47	100.58	100.32	100.97
Formula amounts (*apfu*) (based on the number of oxygen atoms given in the bottom line)										
Ni	0.93	0.87	0.91	0.90	0.86	0.88	0.04	0.03	0.05	0.04
Co^{2+}	0.02									
Fe^{2+}					0.07	0.09				
Ca	0.02		0.01	0.02			0.01	0.01		0.02
Cu^{2+}	0.04	0.04	0.03							
Al	0.05	0.55	0.04	0.04	0.04	0.02	0.09			0.08
V^{3+}							0.05	0.01		
Cr^{3+}	0.05		0.08				1.11	0.01		0.05
Fe^{3+}	1.91	1.51	1.90	2.02			0.67	1.92	1.97	1.75
Ti^{3+}							0.04	0.03		0.04
Si										0.03
Σ	3.02	2.97	2.97	2.98	0.97	0.99	2.01	2.01	2.02	2.01
O	4	4	4	4	1	1	3	3	3	3

[a] Blank cells denote that element contents are below detection limit (<0.05 wt.%). [b] Locality abbreviations: HB – Hatrurim Basin, Negev desert, Israel; DS – Daba-Siwaqa complex, Jordan.

Table 2. Chemical composition of yakubovichite [a]

Locality	Daba-Siwaqa, Jordan (holotype)			Hatrurim Basin, Israel		
	n = 7	range	s.d.	*n* = 8	range	s.d.
Na_2O	1.82	1.35 – 2.18	0.28	1.49	1.30 – 1.75	0.15
K_2O	1.76	1.63 – 2.00	0.16	1.04	0.91 – 1.23	0.11
CaO	6.37	6.07 – 6.88	0.32	7.23	6.74 – 7.91	0.43
SrO	0.49	0.26 – 0.69	0.18	0.39	0.27 – 0.57	0.14
BaO	1.37	1.07 – 1.65	0.20	2.37	2.03 – 2.81	0.31
MgO	2.13	1.24 – 2.88	0.52	3.40	2.93 – 4.11	0.41
CoO				0.06	0.00 – 0.27	0.12
NiO	21.39	20.38 – 22.49	0.68	19.96	18.83 – 21.09	0.68
CuO	0.16	0.00 – 0.37	0.13	0.22	0.00 – 0.48	0.19
Fe_2O_3	18.80	17.76 – 19.45	0.60	18.14	17.2 – 18.95	0.59
Al_2O_3	1.06	0.78 – 1.44	0.23	0.68	0.35 – 0.97	0.19
V_2O_3	0.44	0.26 – 0.71	0.16	0.87	0.44 – 1.47	0.33
Cr_2O_3	0.15	0.00 – 0.49	0.18	0.11	0.00 – 0.17	0.07
SiO_2				0.22	0.00 – 0.42	0.17
TiO_2				0.08	0.00 – 0.26	0.11
P_2O_5	44.15	43.49 – 44.73	0.38	43.85	42.75 – 44.55	0.57
Total	100.09			100.11		

[a] Blank cells denote that element contents are below detection limit (<0.05 wt.%).

Table 3. Scattering factors, site occupancies and bond-valence sums (*v.u.*) for cation sites of yakubovichite from the Daba-Siwaqa complex, Jordan (the holotype)

Site	SC [a]	SOF [b]	SSF [c]	Assigned site occupancy	Site charge	*Z* [d]	BVS [e]
A	Ca, Na	$Ca_{0.78}Na_{0.22}$	18.02	$Ca_{0.51}Na_{0.29}K_{0.18}Ba_{0.04}Sr_{0.02}$	1.56	19.08	1.26
*M*1	Fe, Al	$Fe_{0.90}Al_{0.10}$	24.70	$Fe^{3+}_{0.90}Al_{0.10}$	3.00	24.70	3.07
*M*2	Ni, Mg	$Ni_{0.90}Mg_{0.10}$	26.40	$Ni_{0.72}Mg_{0.13}Fe^{3+}_{0.12}V^{3+}_{0.02}Cu^{2+}_{0.01}$	2.14	25.52	2.11

[a] SC, atomic scattering curves used for site occupancy refinement. [b] SOF, refined site occupancy factor. [c] SSF, refined site-scattering factor (number of electrons per site). [d] *Z*, mean site atomic number calculated from electron microprobe data, normalized to site population = 1. Bond-valence coefficients from Brese and O'Keeffe (1991).

Table 4. Crystal parameters of yakubovichite, its synthetic analogue and related phosphates

	Yakubovichite	**Synthetic**	**Synthetic**	**Xenophyllite**	**Synthetic** [a]
Formula	$CaNi_2Fe^{3+}(PO_4)_3$	$CaNi_2Fe^{3+}(PO_4)_3$	$SrNi_2Fe^{3+}(PO_4)_3$	$Na_4Fe_7(PO_4)_6$	$Na_{1.1}Fe_4(PO_4)_3$
Crystal system	Orthorhombic	Orthorhombic	Orthorhombic	Orthorhombic [b]	Monoclinic
Space group	*Imma*	*Imma*	*Imma*	*Imma* or *Im*2*a* [b]	$P2_1/n$
a (Å)	10.388	10.313	10.388	10.298	6.369
b (Å)	13.088	13.114	13.159	14.997	9.950 [c]
c (Å)	6.479	6.441	6.512	6.351	15.666
V (Å^3)	880.94	871.0	890.2	981.0	992.3
Z	4	4	4	2	4
Reference	This paper	Ouaatta et al. (2017)	Ouaatta et al. (2015)	Britvin et al. (2020)	Zhang et al. (2018)

[a] A likely synthetic analogue of galileiite, $NaFe_4(PO_4)_3$. [b] Body-centered subcell (Britvin et al. 2020d). [c] β = 91.9°.

Table 5. X-ray powder diffraction data (*d* in Å) for holotype yakubovichite [a]

I_{meas}	d_{meas}	I_{calc}	d_{calc}	*hkl*	I_{meas}	d_{meas}	I_{calc}	d_{calc}	*hkl*
5	6.57	2	6.54	020	1	1.813	1	1.814	233
44	5.82	32	5.81	011	14	1.774	4	1.775	361
73	5.51	51	5.50	101			19	1.773	451
32	5.21	33	5.19	200	4	1.757	6	1.755	352
34	4.214	23	4.209	121	2	1.734	3	1.733	512
24	4.075	19	4.068	220	25	1.723	34	1.723	442
13	3.874	16	3.871	211	1	1.695	1	1.698	271
9	3.616	4	3.619	031			2	1.693	541
20	3.239	15	3.240	002	5	1.664	9	1.666	053
20	3.057	18	3.054	301	3	1.637	11	1.636	080
31	3.013	14	3.010	112	4	1.618	7	1.620	004
12	2.889	4	2.903	022	3	1.599	2	1.600	172
9	2.818	7	2.812	141	9	1.586	13	1.586	253
97	2.772	100	2.768	240	3	1.571	3	1.572	024
100	2.748	83	2.749	202	4	1.544	5	1.546	204
38	2.599	41	2.597	400	11	1.528	12	1.530	640
12	2.527	6	2.534	222			12	1.527	602
		8	2.523	132	1	1.484	2	1.485	462
3	2.431	5	2.427	051	1	1.444	3	1.447	701
3	2.231	1.4	2.233	341			1	1.442	381
17	2.201	24	2.199	251	2	1.420	5	1.419	091
18	2.129	16	2.131	013	3	1.409	7	1.410	651
9	2.080	7	2.080	332	7	1.402	14	1.402	453
12	2.033	13	2.034	440	2	1.371	6	1.369	291
7	1.998	6	1.998	152	1	1.362	1	1.362	543
5	1.971	4	1.972	213	2	1.344	3	1.345	424
1	1.893	2	1.894	521	3	1.298	7	1.298	800
6	1.831	6	1.832	303	4	1.266	6	1.267	444

[a] Calculated lines with intensity less than 1 have been omitted.

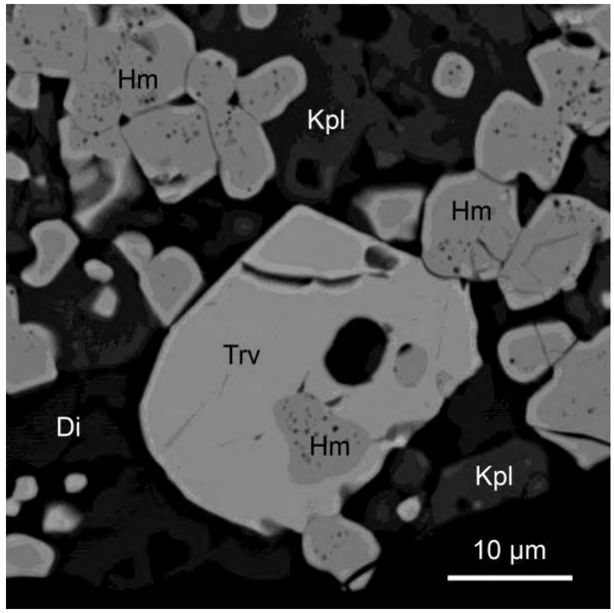

Figure 1.

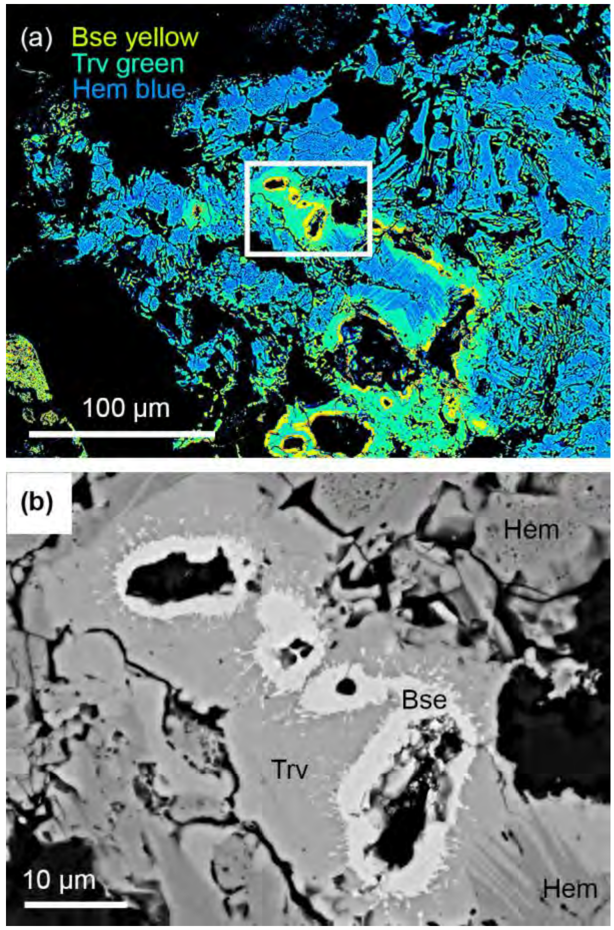

Figure 2.

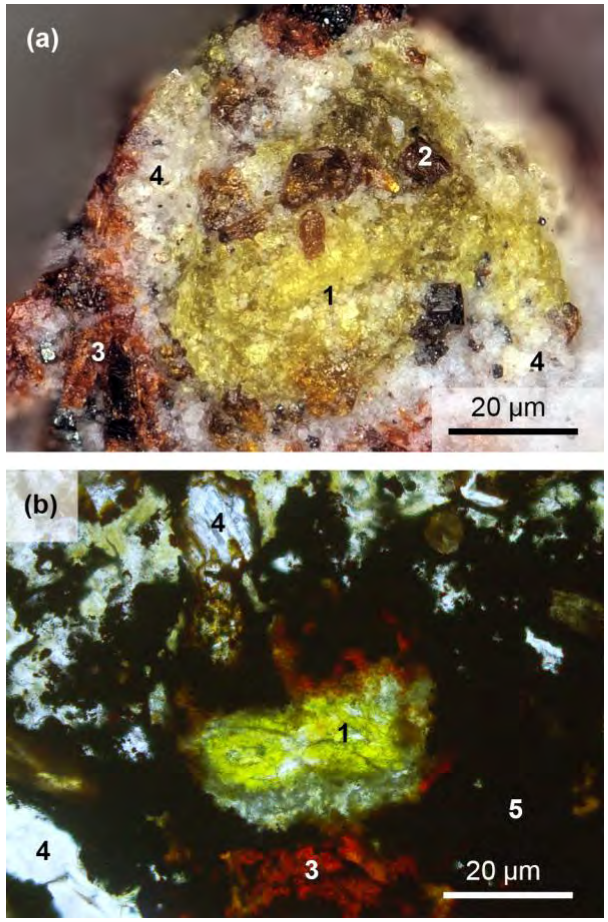

Figure 3.

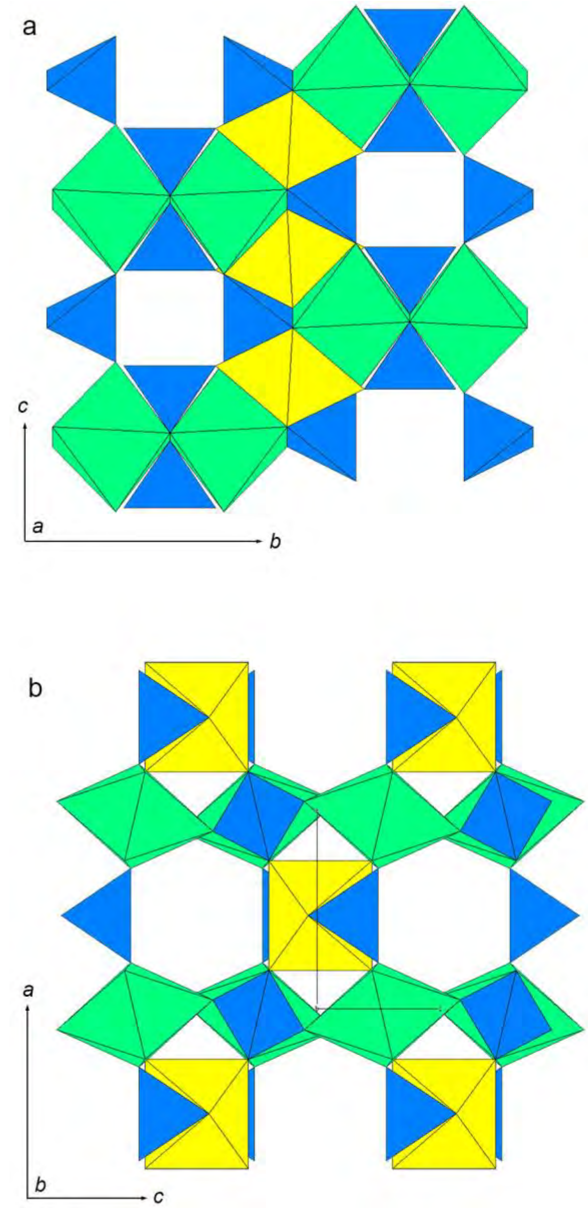

659

660 **Figure 4.**

661

662

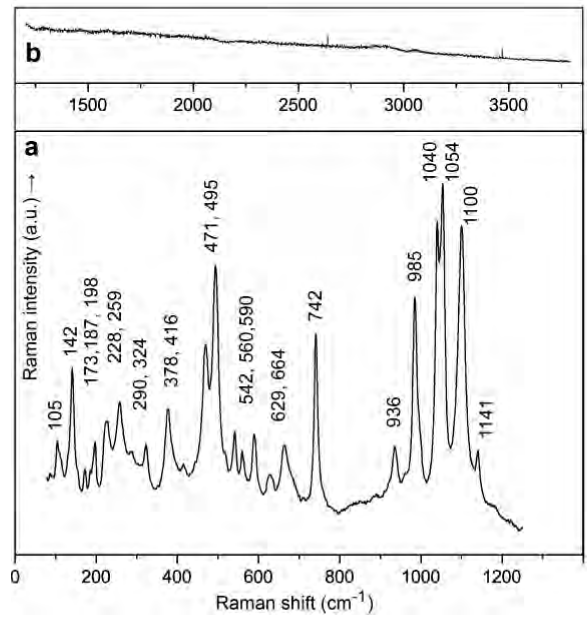
b
1500
2000
2500
3000
3500
a
Raman intensity (a.u.) →
105
142
173,187, 198
228, 259
290, 324
378, 416
471, 495
542, 560,590
629, 664
742
936
985
1040
1054
1100
1141
0
200
400
600
800
1000
1200
Raman shift (cm-1)

Figure 5.

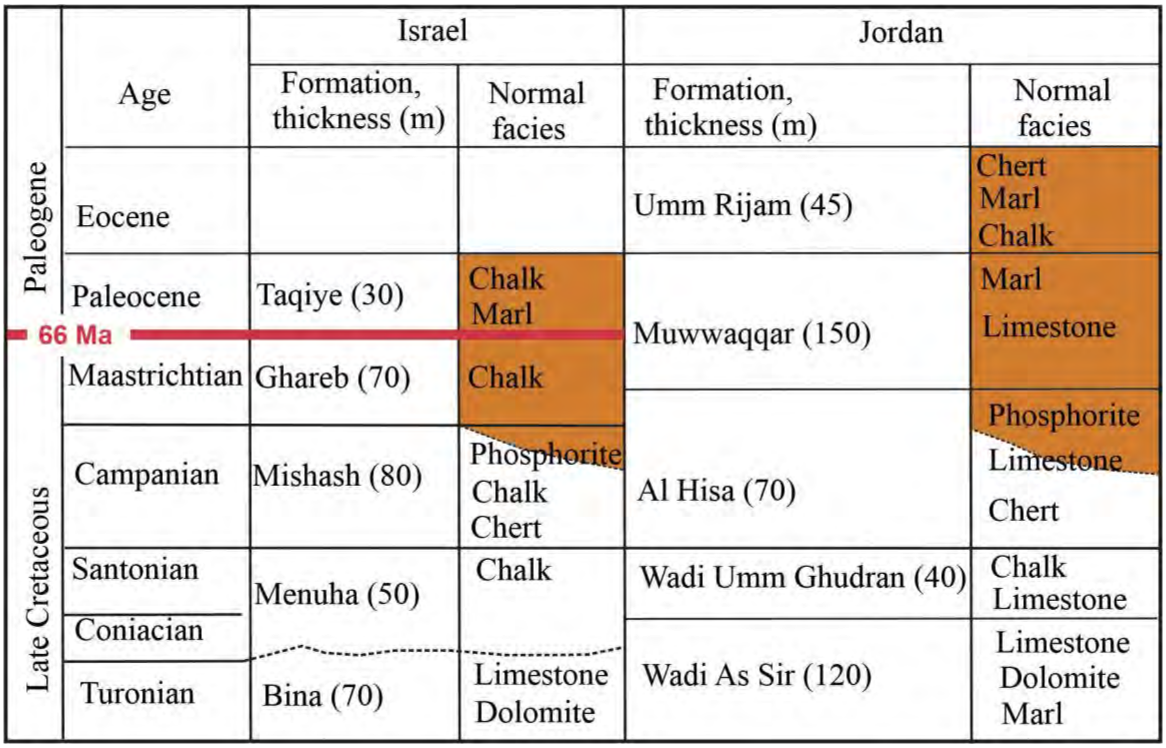
Israel
Jordan
Age
Formation, thickness (m)
Normal facies
Formation, thickness (m)
Normal facies
Paleogene
Late Cretaceous
Eocene
Umm Rijam (45)
Chert
Marl
Chalk
Paleocene
Taqiye (30)
Chalk
Marl
Muwwaqqar (150)
Marl
Limestone
66 Ma
Maastrichtian
Ghareb (70)
Chalk
Campanian
Mishash (80)
Phosphorite
Chalk
Chert
Al Hisa (70)
Phosphorite
Limestone
Chert
Santonian
Coniacian
Menuha (50)
Chalk
Wadi Umm Ghudran (40)
Chalk
Limestone
Turonian
Bina (70)
Limestone
Dolomite
Wadi As Sir (120)
Limestone
Dolomite
Marl

Figure 6.